Materials Advances

ROYAL SOCIETY OF CHEMISTRY

PAPER

View Article Online
View Journal | View Issue

Cite this: *Mater. Adv.*, 2026, 7, 2441

Effect of ammonia borane thermal decomposition under different Ar fluxes on large-area boron nitride films for quantum photonic applications

Elmahdi Amar,[ab] Tiago Queirós,[ab] Nicoleta Nicoara,[a] Siva S. Nemala,[a] Diego A. Garzón,[a] James C. Peters,[ab] Jana B. Nieder,[a] Pedro Alpuim,[a] Carlos J. Tavares[ab] and Sascha Sadewasser *[a]

Hexagonal boron nitride (h-BN) has emerged as a promising 2D material. It has a wide band gap (~6 eV), which can host numerous optically active structural defects. Here, a detailed investigation is presented on the growth of BN films using ammonia borane NH_3BH_3 (AB) powder as a precursor. The growth is performed *via* atmospheric pressure chemical vapor deposition (AP-CVD) where AB thermal decomposition under Ar flow is considered as a vital step for the deposition of high-quality BN. In this context, the AB pre-treatment step is tuned by testing two different Ar gas flow conditions: low flux (5 sccm), and high flux (95 sccm). BN thin films are grown and successfully transferred onto SiO_2/Si, glass, and sapphire substrates using a wet chemical method. X-ray photoelectron spectroscopy shows similar surface chemical composition of the BN films. Large-area BN films (~1 cm^2) with a thickness of 7 nm are confirmed by atomic force microscopy and X-ray reflectivity. From the transmittance and reflectance curves, and respective Tauc plots, the estimated band gaps are in the range of 3.73 to 5.02 eV. Fluorescent spots observed in BN thin films in the wavelength range of 520 to 696 nm exhibit blinking events. This fluorescence intermittency observed *via* total internal reflection fluorescence microscopy (TIRF), indicates that AP-CVD grown BN may foster defects that can act as single photon emitters (SPEs). These studies will enable the optimization of h-BN production, aiming to get high-quality SPEs in h-BN for future quantum technology application.

Received 3rd June 2025,
Accepted 20th January 2026

DOI: 10.1039/d5ma00584a

rsc.li/materials-advances

1. Introduction

Boron nitride (BN) with either sp^2 or sp^3 bonding can generate a variety of BN polytypes. Cubic (c-BN) and wurtzite (w-BN) phases have sp^3-hybridized bonds. Hexagonal (h-BN), turbostratic (t-BN) or rhombohedral (r-BN) phases are constructed by flat layers of atoms of sp^2 bonds, with a large separation between two layers joined by van der Waals forces.[1,2] 2D hexagonal boron nitride (h-BN) is a van der Waals material with insulating properties that possesses a honeycomb crystal structure similar to that of graphene but with a slight mismatch of the lattice constants.[3] It is flat, strong, and relatively free of dangling bonds, when compared with other substrates such as SiO_2.[4] CVD growth of h-BN films may follow an island growth instead of layer-by-layer growth model.[5] h-BN as an emerging 2D material has remarkable properties,[6,7] such as a large band gap (~6.0 eV), excellent thermal and chemical stability, high thermal conductivity, and its significant potential as an indispensable dielectric layer in high-performance 2D integrated electronics.[8–11] Atomically thin 2D materials can be prepared through different strategies, including mechanical exfoliation,[12] liquid-phase exfoliation,[13] CVD,[14] pulsed laser deposition (PLD),[15] and molecular beam epitaxy (MBE).[4] CVD is the most common technique for fabricating high-quality and large-scale 2D thin films.[16–20] A CVD reactor uses gaseous precursors to react on the surface of a substrate and grows thin films of micrometer-scale with high uniformity.

It is interesting to note that h-BN films can be stable at 1500 °C in air.[21,22] In addition, h-BN layers can serve as high-performance coatings, capable of resisting oxidation up to 1100 °C.[21] Its physical and chemical characteristics favor its use as a passivation layer[21,23] or deep ultraviolet emitter.[24,25] For more than a decade, h-BN was used as a thermally stable ceramic material. More recently, it has been employed as an ideal substrate for graphene due to its atomic flatness.[8] Previous literature highlights that h-BN can host various defects, including strain,[26,27] edges/grain boundaries,[28] B vacancies,[29]

[a] *INL-International Iberian Nanotechnology Laboratory, 4715-330 Braga, Portugal. E-mail: Sascha.Sadewasser@inl.int*
[b] *Physics Center of Minho and Porto Universities (CF-UM-UP), University of Minho, 4710-057 Braga, Portugal*

N vacancies,[30] among others. These defects are a probable source of room-temperature quantum emitters. However, carbon contamination cannot be excluded as a candidate, as it may introduce emissive defect states. For example, Zhong *et al.*[12] recently reported single photon emission (SPE) in h-BN flakes created *via* carbon implantation. Nowadays, this 2D material is considered a promising candidate for the next generation of SPEs, paving the way for applications in quantum optics and nanophotonics.[31,32]

Atmospheric pressure chemical vapor deposition (AP-CVD) is a promising method in which scalable high-quality films can be grown at reasonable cost. However, several parameters influence this growth process, including temperature, growth time, precursor weight, substrate cleaning, choice of precursor, and gas flow rate. The chemical vapor deposition (CVD) growth of h-BN from ammonia-borane is typically carried out in the presence of Ar:H_2 mixture, it gives variable results depending on the growth temperature,[33] working pressure in CVD conditions,[34] and time dependent decomposition of the ammonia borane precursor.[35] In this framework, a series of experiments were conducted using an AP-CVD system to optimize the growth process. The crucial parameters were varied systematically to avoid copper oxide, carbon contamination, helically wrapped Cu foil issues during quenching, and non-homogeneity of BN films. Several studies have demonstrated that h-BN films can be effectively synthesized *via* CVD in Ar:H_2 gas mixture environments. During the thermal decomposition phase, ammonia borane (AB) typically breaks down under either H_2,[36,37] Ar:N_2,[5] or Ar:H_2 gas mixture,[34,35,38] releasing species such as H_2, borazine, polyaminoborane, and polyiminoborane. These decomposition products play a crucial role in regulating the growth rate and nucleation density of BN grains. In our approach, we introduce a novel pre-treatment of the AB precursor using only argon under both low flux (LF) and high flux (HF) conditions, without hydrogen gas. This method has not been previously reported. Using Ar as the carrier gas at this stage ensures an inert atmosphere, thereby eliminating the need for H_2 during the AB thermal decomposition. Tuning this Ar flux may influence reaction kinetics, and the density of point defects, enabling viability of the fabricated AP-CVD thin BN ($\sim$7 nm), as a SPE platform. 2D materials grown on a substrate are sensitive to surface impurities and local growth conditions. A 95 : 5% Ar : H_2 gas mixture provides stable flow conditions and suppresses unwanted reactions at elevated temperatures ($\sim$1020 °C).[39,40] Hydrogen is maintained at 5% because it effectively prevents Cu oxidation and keeps its surface clean during heating.[41] From previous reports, CVD growth with higher H_2 fluxes of 7 sccm and 9 sccm at constant Ar flux of 95 sccm leads to excessive etching of BN layers.[42] Therefore, controlling thin-layered BN films using AP-CVD requires a special precaution to ensure a consistent quality of BN.

In this study, a synthesis method for large-scale BN films ($\sim$1 cm^2) uses a Cu foil and ammonia borane precursors. The growth is executed through an AP-CVD system with two heating zones under a mixture of Ar : H_2 with flow rates of 95 : 5 sccm. Prior to the BN effective growth, an AB pre-treatment at 110 °C creates an adequate environment to produce various chemical compounds from the precursor. Nevertheless, other parameters in AP-CVD growth can induce a significant amount of lattice distortions, which affect the quality of BN films. The controlled synthesis of BN thin films involves precise adjustment of ammonia borane sublimation during the AB pre-treatment process. The synthesis of uniform BN multilayers remains challenging due to the difficulty in controlling the various solid-phase species that emerge during each stage of AB decomposition.[43] The thermal decomposition of the AB precursor is analysed by Fourier-transform infrared spectroscopy (FT-IR). The quality and uniformity of BN films are analyzed by Raman spectroscopy. The film thickness is determined by atomic force microscopy (AFM) and X-ray reflectivity (XRR). The bonding state and chemical composition of BN films are obtained from X-ray photoelectron spectroscopy (XPS). In addition, total internal reflection fluorescence (TIRF) microscopy and hyperspectral confocal fluorescence imaging (HCFM) are used to study the fluorescence of emitters in atomically thin BN films. Finally, the statistical analysis of fluorescence intermittency indicates the presence of room temperature photon emitters in BN films, making this material interesting for quantum technologies. The presented findings advance the understanding of BN synthesis using AP-CVD to establish an optimized industrial process of 2D materials growth.

2. Material and methods

2.1 Growth of BN films using AP-CVD

A home-built atmospheric pressure chemical vapor deposition (AP-CVD) system is used to synthesize multilayers of BN on copper foil (Fig. 1a).

The system consists of a cylindrical quartz tube with an inner diameter of 1 inch (length: 120 cm), placed inside two programmable hot-wall furnaces (Furnace 1: Lindberg Blue-M; Furnace 2: Termolab). A 25 μm thick Cu foil is used as substrate

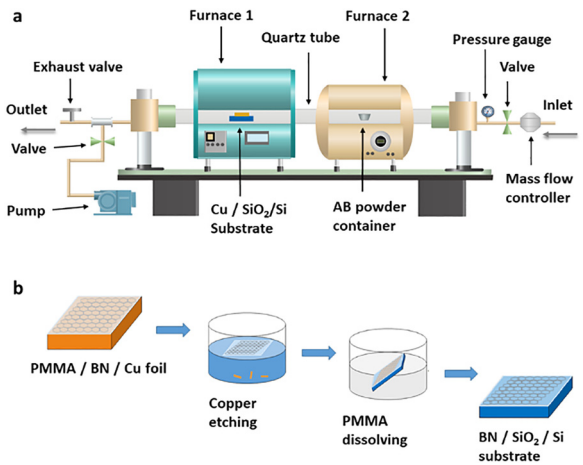

Fig. 1 (a) Schematic illustration of the AP-CVD synthesis setup of BN. (b) Main steps involved in the transfer of BN films onto a SiO_2/Si substrate by wet chemical method.

(99.99% purity, Sigma-Aldrich). Ammonia borane (NH_3BH_3) is employed as the single-source precursor and placed approximately 50 cm away from the Cu foil substrate inside the quartz tube. Before BN deposition, the Cu substrate is cleaned by ultrasonication in an aqueous solution (280 ml deionized water (DI), 10 ml HCl 37%, 2.5 ml 0.5 M $FeCl_3$) for 2 min, and then rinsed twice in DI water for 2 min, placed on a cleaned SiO_2/Si holder (5 cm × 2 cm), and loaded into the first heating zone (Furnace 1). 17 mg of AB powder is positioned in a small Al container in the second heating zone (Furnace 2). The system is initially pumped down to 3.9×10^{-3} mbar with the exhaust valve closed, which allows removal of air (or unwanted impurities) in the gas line and the quartz tube. Then, the tube is purged for 10 min under a gas mixture of 95 sccm Ar and 5 sccm H_2. After purging, the temperature of the furnace 1 is ramped up to 1020 °C (20 °C min^{-1}) to anneal the copper foil for 40 minutes under the same Ar : H_2 (95 : 5 sccm) gas mixture, with the exhaust valve open. This annealing step is carried out at approximately atmospheric pressure. It partially restricts oxidation of the Cu foil surface. Then, the Cu substrate is left to cool down to room temperature by opening the Furnace 1 lid (Furnace 1 OFF). Next, the AB is heated to 110 °C using Furnace 2 for AB pre-treatment under the selected Ar flow (Table 1). The AB pre-treatment process is conducted for 150 min with the exhaust valve closed. This step is confirmed to be crucial for high-quality BN films (Fig. S1).

Two distinct samples were grown on Cu foil using two different Ar flow rates during AB pre-treatment, sample BN-LF with low flow (5 sccm) and sample BN-HF with high flow (95 sccm). During this step, the AB precursor undergoes initial decompositions between 100–120 °C (details in Fig. S2), resulting in a pressure increase up to ~1200 mbar and ~3000 mbar for 5 sccm and 95 sccm of Ar, respectively (Furnace 2 ON and Furnace 1 OFF, see Table 1). After completing the AB pre-treatment, an Ar : H_2 gas mixture (95 : 5 sccm) is introduced while maintaining Furnace 2 at ~110 °C. Simultaneously, Furnace 1 is ramped up again to 1020 °C (20 °C min^{-1}) with the exhaust valve open, restoring pressure to atmospheric level. The effective BN growth lasts for 30 min under continuous Ar : H_2 flow of 95 : 5 sccm (see SI, Fig. S1). Finally, both furnaces are switched off to cool down the sample and the precursor to room temperature. The temperature variation over time during the growth process is displayed in Fig. S1 (SI). The growth condition details of BN films used in this study are summarized in Table 1.

2.2 Transfer process of BN film onto substrates

The as-grown BN film is transferred onto a 300 nm SiO_2/Si (Fig. 1b), and also onto glass and sapphire substrates, depending on the intended characterization technique. A supporting layer of polymethyl methacrylate (PMMA) is produced using a spin coater. The back side of the PMMA/BN/Cu stack is cleaned *via* O_2 plasma (250 sccm O_2 flow, four consecutive cycles of 30 s plasma exposure, 250 W RF power) to remove any unwanted BN depositions. Afterwards, the PMMA/BN/Cu stack is immersed for 90 min in a 0.2 M $FeCl_3$ solution to etch away the copper. The floating PMMA/BN film is subsequently picked up from the solution with a SiO_2/Si, glass or sapphire substrate and washed twice with DI water. The sample is left to dry for 12 hours for better adhesion. Next, it is subjected to a cleaning process by dipping it in acetone for 60 min to dissolve PMMA and effectively remove any unwanted contaminants. The last steps include cleaning of the sample with isopropyl alcohol (IPA) and rinsing with DI water for 15 min each. Finally, the sample is subjected to ultrasonication in DI water for 5 min, followed by gentle drying under a N_2 flow.

2.3 Materials characterization

Fourier transform infrared spectroscopy (FT-IR) of ammonia borane powder samples were collected on a Bruker IFS55 FT-IR spectrometer (attenuated total reflectance (ATR) FT-IR spectroscopy), using a single reflectance ATR cell (Golden Gate,

Table 1 Summary of growth conditions for the BN films grown *via* AP-CVD for BN-LF (low flux) and BN-HF (high flux). F1 and F2 indicate Furnace 1 and Furnace 2, respectively

Step	Gas inlet	Pump valve	Exhaust outlet	Parameters	BN-LF	BN-HF
Purge	Open	Open	Closed	Gas flow (sccm)	Ar : H_2 (95 : 5)	
				Duration (min)	10	
F1. OFF				Temperature F1 (°C)	RT	
F2. OFF				Temperature F2 (°C)	RT	
Annealing	Open	Closed	Open	Gas flow (sccm)	Ar : H_2 (95 : 5)	
				Duration (min)	40	
F1. ON				Temperature F1 (°C)	1020	
F2. OFF				Temperature F2 (°C)	RT	
AB-pre-treatment	Open	Closed	Closed	Gas flow (sccm)	Low flux Ar (5)	High flux Ar (95)
				Duration (min)	150	
F1. OFF				Temperature F1 (°C)	RT	
F2. ON				Temperature F2 (°C)	110	
BN growth	Open	Closed	Open	Gas flow (sccm)	Ar : H_2 (95 : 5)	
				Duration (min)	30	
F1. ON				Temperature F1 (°C)	1020	
F2. ON				Temperature F2 (°C)	110	

equipped with a diamond crystal). All data were recorded at room temperature, in the spectral range of 4000–400 cm^{-1}, by accumulating 16 scans with a resolution of 4 cm^{-1}. Three spectra were collected for each sample to evaluate experimental reproducibility.

Raman spectroscopy was performed with an ALPHA300 R Confocal Raman Microscope (WITec) using 532 nm laser light for excitation at room temperature. The laser beam was focused on the sample with a 50× lens (Zeiss). Single acquisitions were performed using a 600 g mm^{-1} grating and with a laser power of 17.5 mW.

Scanning electron microscopy (SEM) micrographs were acquired using a FEI Quanta 650 FEG with a cold field electron source, using an electron acceleration voltage between 5 kV and 10 kV at a 10 mm working distance in high vacuum.

Atomic force microscopy (AFM) was performed with a Bruker Dimension ICON in tapping mode, using Pt/Ir-coated Si cantilever tips (resonant frequency ~300 kHz). Image processing was done with Gwyddion and WSxM softwares.

X-ray photoelectron spectroscopy (XPS) was performed with an ESCALAB 250 XI (Thermo Fisher Scientific, source: Al Kα 1486.6 eV, 650 μm spot size, pass energy: 40 eV with hemispherical analyzer) system under ultrahigh vacuum (~5×10^{-10} mbar) conditions. A dual beam consisting of Ar^+ ions (0.5 keV) and electrons (0.5 keV) was used to clean the surface of the studied samples.

Transmittance and reflectance were measured in a UV-VIS-NIR Spectrophotometer (PerkinElmer – Lambda 950) with integrating sphere detector in the wavelength range from 180 to 380 nm.

X-ray reflectivity (XRR) experiments were performed using a Bruker AXS D8 Discover diffractometer, employing Cu K_α radiation. A high gain Göbel type X-ray mirror was placed in front of the incident beam, with a minimum length of 40 mm and divergence of below 0.03°, while on the detection side Soller slits were used for parallel beam with angular resolution between 0.2° and 0.3°. A knife edge was placed 50 μm above the sample surface.

Time dependent fluorescence emission studies were performed using a Nikon Ti-E widefield total internal reflection fluorescence (TIRF) microscope with a 488 nm laser at 25 mW average power. The setup included an incubator chamber housing a motorized XY stage coupled with a sensitive motorized piezo Z stage (minimum step of 0.025 μm). The fluorescence emission signals were captured in a wavelength range from 482 to 700 nm using a dichroic beamsplitter (Di02-R532-25×36, Semrock). A cube filter with excitation (482/18 nm) and emission (525/45 nm) band-pass filters was placed in front of an Andor IXon Ultra 897 EMCCD camera with an integration period of 50 ms per frame. An oil immersion lens with 60× magnification and 1.4 NA (Plan Apo 60× Oil DIC H N2) was employed. Measurements using wide-field TIRF were performed on sample regions of 136 μm^2. Within the most focused portion of the recordings, four smaller regions of interest, measuring 8 μm^2, were chosen for each of these locations. The ThunderSTORM plugin in ImageJ was utilized for image processing to locate intensity of bright spots. The point spread function (PSF) was used to extract locations of single or few fluorescence emitters in the TIRF micrographs. For each of the extracted positions, the time-dependent fluorescence intensity was extracted and analyzed in terms of their intermittency characteristics.

Hyperspectral confocal fluorescence microscopy (HCFM) investigation was carried out using a Zeiss LSM 780 confocal microscope, equipped with a 32-channel GaAsP detector for spectral imaging. This microscope equipped with a 63× magnification oil immersion objective (1.4 NA, Plan Apochromat, DIC M27, Zeiss) was used to collect the signal (the PSF of the system had a 220 nm FWHM for 488 nm wavelength). The detector was configured to cover emission wavelengths between 520 and 696 nm. Argon laser emission at 488 nm was used to excite the BN samples at 12.5 mW average power. High spectral resolution images of 45 μm^2 were acquired pixel by pixel in laser scanning mode. The signal was averaged 16 times with approximately 50 μs collection time per pixel (with an integration time of 0.8 ms per pixel). ImageJ was used to segment the linear unmixed channels into signal and background *via* thresholding, and to perform quantitative analysis of diffraction-limited spots, which were used to identify fluorescent spots (emitters) per unit area.

3. Results and discussion

3.1 Ammonia borane thermal decomposition

Ammonia borane (NH_3BH_3, AB) powder is considered an emerging material for hydrogen storage, with a high hydrogen content (19.6 mass%), as well as having assured stability.[44,45] When AB breaks down at high temperatures (solid–gas reaction), hydrogen is released from the powder in several steps. This leads to the creation of polyaminoborane ($(NH_2BH_2)_n$, PAB), polyiminoborane ($(NHBH)_n$, PIB), and finally boron nitride (BN) (Fig. S2, SI). Fig. 2a shows a photo of the pure AB powder (left side) and how it agglomerates at the end of the growth process (right side).

FT-IR spectra of pristine ammonia borane and post-heated powders referred to as AB_BN-LF and AB_BN-HF were recorded as shown in Fig. 2b. The results show the characteristic bands

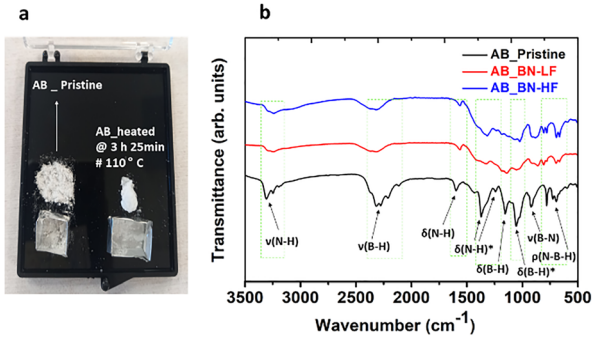

Fig. 2 (a) Photograph of pristine AB powder and post-heated powder at the end of the growth. (b) Fourier-transform infrared (FT-IR) spectra of pristine ammonia borane NH_3–BH_3 (commercial sample with purity >97% from Sigma-Aldrich), for AB_BN-LF, and AB_BN-HF post-heated powders.

of the stretching mode ν(N–H) at 3406–3250 cm^{-1}, indicating the formation of a (NH_2BH_2) type structure or terminal NH_2 groups.[43] Another mode ν(B–H) at 2378–2120 cm^{-1} may involve BH_3 and BH_2 vibrations.[46] The bending modes δ(N–H) and δ(N–H)* indicated in a range of 1630–1597 cm^{-1} and 1404–1351 cm^{-1}, respectively, are assigned to the umbrella vibration mode of the terminal NH_3 group,[45] and δ(B–H) seen at 1235 cm^{-1} can possibly involve unresolved bending modes, including BH_2 deformation and BH_3 umbrella.[43]

Additionally, two more relevant core peaks are identified at 1115 cm^{-1} and 788 cm^{-1}, which are supposed to be associated with δ(B–H)* (rocking vibrations) and ν(B–N) (stretching vibrations), respectively.[47] These vibrational modes of the pristine ammonia borane vanish in case of AB_BN-LF and AB_BN-HF post-heated powders, indicating that they are partially decomposed. The decrease in the intensity of two broad bands centred at 3406–3250 cm^{-1} and 2378–2120 cm^{-1} may indicate the presence of B–H bonds due to the formation of polyaminoborane and polyiminoborane. The disappearance of the above-mentioned 1235 cm^{-1} bands indicates the rupture of the B–H bond due to H_2 release. The peak at 788 cm^{-1} corresponding to ν(B–N) bending mode disappears in both post-heated powders because of the significant rupture of B–N bonds. Moreover, it is noteworthy that the strength of the peak's shoulders is in the region between 633 and 790 cm^{-1} for AB_BN-HF post-heated powder compared to AB_BN-LF, demonstrating that the ρ(N–B–H) rocking bond is still intact at AB_BN-HF similarly to the one in the pristine AB precursor.

3.2 BN film structural analysis

The as-grown BN films were transferred to various substrates through a wet chemical process. Fig. 3a presents the centimeter-scale of the BN-LF thin films; the homogenous blue color in the middle indicates the area of BN films (1 cm^2) that was transferred onto a SiO_2/Si substrate. The SEM micrograph in Fig. 3b shows BN-LF nucleation sites associated with an irregular grain distribution. In contrast, the SEM micrograph of BN-HF (Fig. 3c) reveals agglomerated grains that form continuous BN islands.

This difference may be attributed to the increased argon flux used during the AB pre-treatment, slight differences in the distance between the AB precursor and the Cu substrate, and possibly some secondary nucleation events. Additionally, a minor variation of the vapor pressure, temperature gradients, and diffusion patterns during the growth process could give rise to different sizes of BN grains. During the transfer process, sometimes the BN layers fold onto themselves, as shown in the optical micrograph for the BN-LF/SiO_2/Si sample (Fig. 3d). Nevertheless, the BN thin film is evidently distinguishable from the SiO_2/Si substrate, with a clear boundary between the film and the substrate. In other cases, some wrinkles in the BN films are observed, as shown for the sample BN-HF/SiO_2/Si in Fig. 3e. Wrinkles are more evident on the surface, as they might be induced by mechanical strain effects during the transfer process, especially when the samples are cut for the Cu foil dissolution in $FeCl_3$ (more details in the SI). Moreover, we have tested various BN/Cu samples with Raman spectroscopy. However, BN-LF films on Cu foil did not yield a useful Raman signal due to reflection by the Cu background.

Fig. 3f shows Raman spectra collected from different positions (p1 and p2) of both samples (BN-LF and BN-HF) on SiO_2/Si substrates. A sharp peak at 1370 cm^{-1} is observed, corresponding to the in-plane E_{2g} phonon vibration of BN. The peak at 1450 cm^{-1} is assigned to the third-order transverse optical

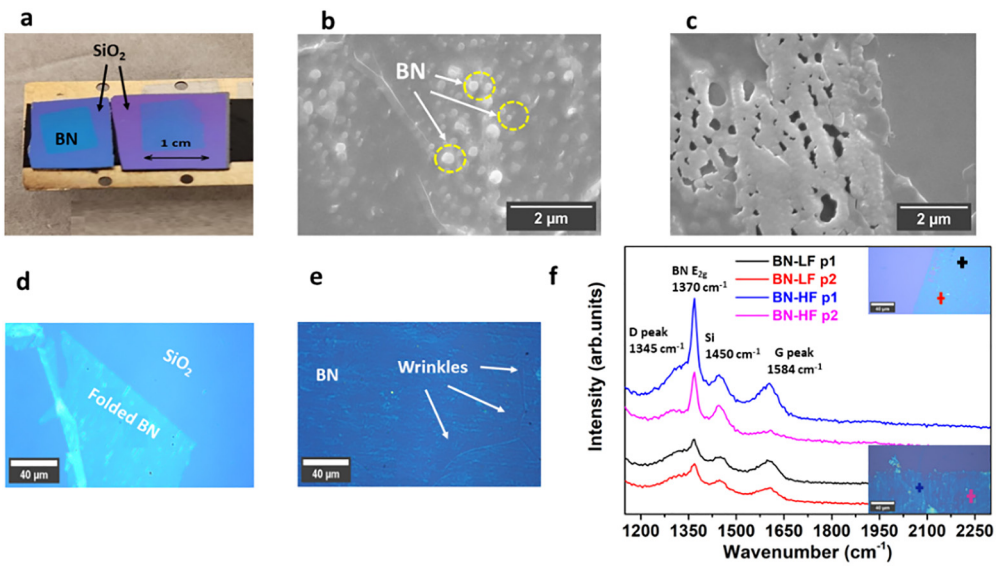

Fig. 3 (a) Photograph of BN-LF thin film transferred onto a SiO_2/Si substrate (1 cm^2). (b) The dashed yellow circles in the SEM micrograph show the BN-LF nucleation sites for a growth time of 30 min. (c) SEM image showing the formation of continuous BN-HF islands (30 min deposition). (d) Optical micrograph of the BN-LF films transferred onto SiO_2/Si showing folded BN sheets. (e) Optical micrograph of the BN-HF films transferred onto SiO_2/Si showing wrinkles indicated by white arrows. (f) Raman spectra for BN films collected at the positions marked with crosses in the insets. The color of the Raman spectra corresponds to the color of the (+) symbols.

phonon mode of the SiO_2/Si substrate. However, it is clearly seen that there are some residual D (1345 cm^{-1}) and G (1584 cm^{-1}) carbon-related bands with slight differences in intensities, which could be attributed to minor carbon contaminations from the tube furnace seals. These carbon contaminations appear to be inhomogeneous as suggested by varying peak intensities.

3.3 BN film topography

Atomic force microscopy (AFM) is used to further characterize the BN films. Fig. 4a displays an AFM topography image of the transferred BN-LF films on a SiO_2/Si substrate. BN islands have few cracks which were generated due to the transfer processes. The inset in Fig. 4a shows an optical micrograph of the sample's scanned area, where the BN islands can be identified due to a contrast difference with respect to the SiO_2/Si substrate. The measured thickness of the BN-LF films is approximately (7.0 ± 0.1) nm (~17 layers) (Fig. 4b). On the other hand, it is known that wrinkles can be created because of the bending of the top layers and the adhesion between BN layers and the substrate. Herein, the AFM image of sample BN-HF in Fig. 4c shows some wrinkles, which we assign to issues that sometimes occur during the transfer process. In addition, wrinkles can also be formed because of thermal expansion between BN film and the Cu foil[48] (*i.e.*, since the BN-LF thin films are grown on Cu at high temperature of 1020 °C, when the substrate is cooled to room temperature, the Cu shrinks but the BN expands forming wrinkles).[49] Another possible reason for this may be a strain relaxation between PMMA/BN and Cu interfaces, which is likely to be present after the PMMA spin coating process. As a result, an increased number of folds and structural defects may be expected. Fig. 4f depicts the surface roughness average of a small area from the BN-LF film (Fig. 4e), which is analyzed in comparison to roughness extracted from small area of SiO_2/Si (Fig. 4d) by fitting topography histograms with a Gaussian distribution, leading to RMS values of (2.7 ± 0.1) nm and (1.9 ± 0.1) nm, respectively (Fig. 4f). The measured surface roughness for BN thin layers in various areas are slightly different which can be ascribed to the Cu foil with its densely packed rolling lines imprinted on it.

The statistical analysis indicates that the transferred BN-LF flakes show some step-heights ranging from (1.1 ± 0.1) nm (~3 layers) to (1.8 ± 0.1) nm (~5 layers), as determined from the black line profile in Fig. 4b. Moreover, the AFM profile (shown in cyan in Fig. S4b, SI) measures a thickness of (7.5 ± 0.1) nm (~18 layers) for the BN-HF film, with RMS values of 2.4 nm for BN layers and 1.6 nm for SiO_2 (see Fig. S4a in the SI). The thickness of a single monolayer (1 ML) is ~0.42 nm.[50]

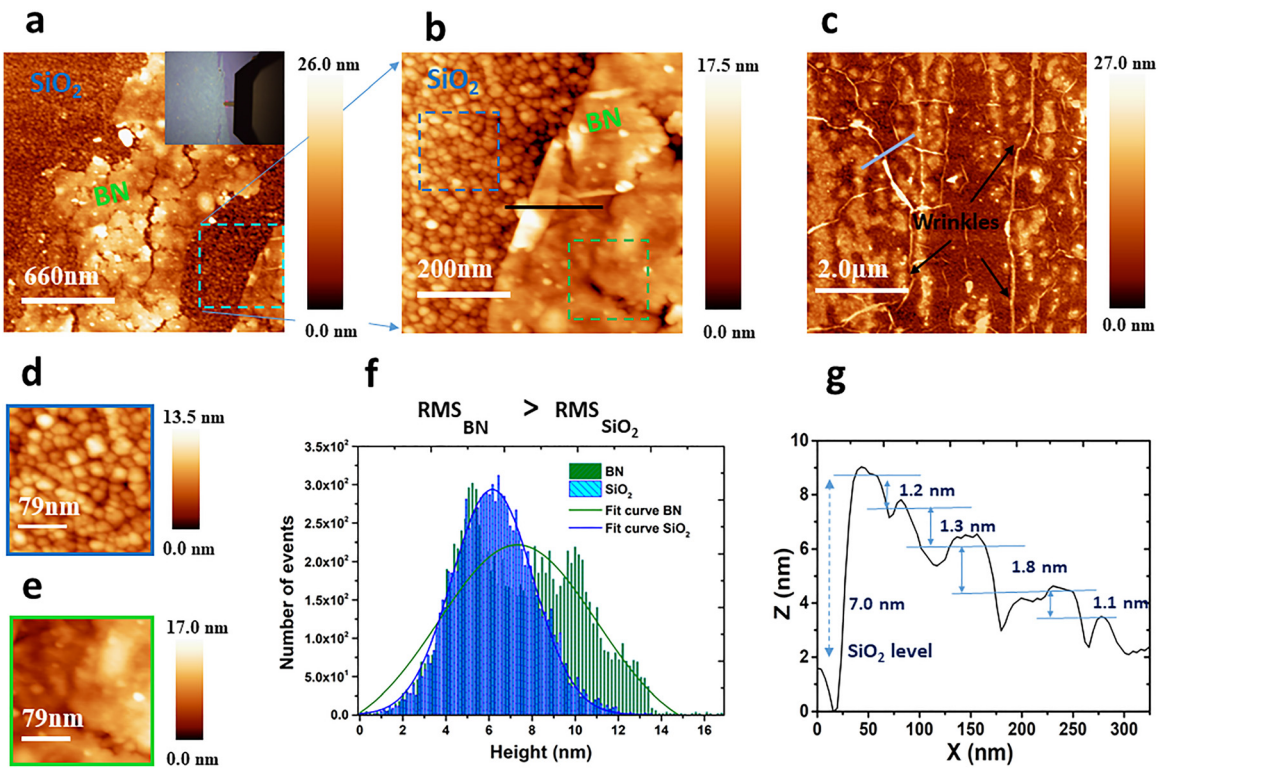

Fig. 4 (a) AFM topography scans of the transferred BN films (BN-LF/SiO_2/Si); the inset shows an optical image of the scanned area. (b) AFM topography of BN islands (BN-LF/SiO_2/Si); (c) presence of wrinkles over the scanned area in the sample BN-HF/SiO_2/Si; line-scan profile indicating a thickness of 7.5 nm. (d) and (e) High resolution topography of SiO_2/Si (blue square) and BN-LF (green square) selected areas. (f) Roughness histogram profiles extracted from BN-LF covered area and from SiO_2/Si area and their respective fits with a Gaussian distribution (blue and green lines). (g) Height profile of BN along the black solid line in (b), indicating a thickness of 7 nm and showing distinct step-heights of the BN-LF with thin layers of 1.2 nm, 1.3 nm, 1.8 nm and 1.1 nm.

The observed discrepancy in thickness between the BN-LF and BN-HF films is attributed to variation in the number of layers. However, we cannot exclude the presence of some contamination by remnants of the PMMA polymer or unwanted impurities. These impurities might have accumulated in certain areas of the BN-HF flakes during the final cleaning processes (Fig. 4c).

3.4 BN atomic composition analysis

X-ray photoelectron spectroscopy (XPS) is performed to investigate the atomic composition as well as the chemical bonding environment of the BN samples. XPS measurements are carried out for as-grown BN-LF films on Cu foil just after the AP-CVD growth, and for BN films after transfer to SiO_2/Si substrates. Fig. S5 shows the XPS survey spectrum of the as-grown BN-LF film on Cu foil, which is different to those from BN thin films on SiO_2/Si substrates (SI).

The high-resolution binding energy scans investigate the chemical states of the B, O, C, and N atoms in the as-synthesized BN films on Cu foil and in BN-LF and BN-HF on SiO_2/Si. The O 1s, N 1s, and B 1s core line levels are corrected with respect to the binding energy of the C 1s peak (C═C bond) at 284.84 eV.[51,52] The observed intensity of C 1s originates possibly from the furnace seals, which decompose at high temperatures, releasing carbon-containing impurities. The high-resolution XPS peaks of B 1s, O 1s, C 1s, and N 1s core levels are deconvoluted using Gaussian–Lorentzian fitting (red, magenta, green, and blue peaks) to extract different contributions from each spectrum.[53] Thus, for the samples (as-grown BN-LF/Cu, BN-LF/SiO_2/Si), the observed binding energies of O 1s at 531.60 and 532.64 eV can be ascribed to O–C and O–B bonds, respectively (Fig. 5a and e).[13,54,55] It is clearly seen that the peak positions of O–B and B–OH (534.23 eV) bonds are constant for all samples; their origin can be related to sp^3-hybridized $N_3B(OH)$ formed during ultrasonication of the BN layers in DI water,[13] or due to oxygen diffusion from the SiO_2/Si substrate holder. Furthermore, the back side of the Cu foil was exposed to an oxygen plasma to remove unwanted BN film, which might be a further source of oxygen. In addition to the C═C bonds, two other peaks arise in the C 1s spectra of all samples, at 286.55 and 288.70 eV, which correspond to C–N and C═O bonds, respectively (Fig. 5c, g and k).[55,56] The peak corresponding to the C═O bond is associated with sp^2 C–O bonding, likely due to the presence of adsorbed CO and CO_2 originating from the ambient atmosphere. This peak position is invariant in all samples, which indicates identical C═O chemical states. Moreover, in the case of the N 1s (Fig. 5b) core line for as-grown BN-LF/Cu, the peaks at the binding energies of 398.61 and 400.11 eV correspond to N–B, N–C bonds, respectively.[57,58] Similarly, for this sample, Fig. 5d shows the peaks at 190.77, 191.59 and 193.54 eV in the B 1s core line, which are attributed to B–N, C–B–N, and B–O bonds, respectively.[58,59] Furthermore, in the case of BN-LF(HF)/SiO_2/Si samples, the N 1s peak is shifted towards lower binding energies (398.17 eV) due to N–B bonding (Fig. 5f and j).[57,60] However, for the latter samples, both peaks B–N and C–B–N observed in the B 1s core line are shifted towards smaller binding energies at 190.44 eV and 191.16 eV, respectively

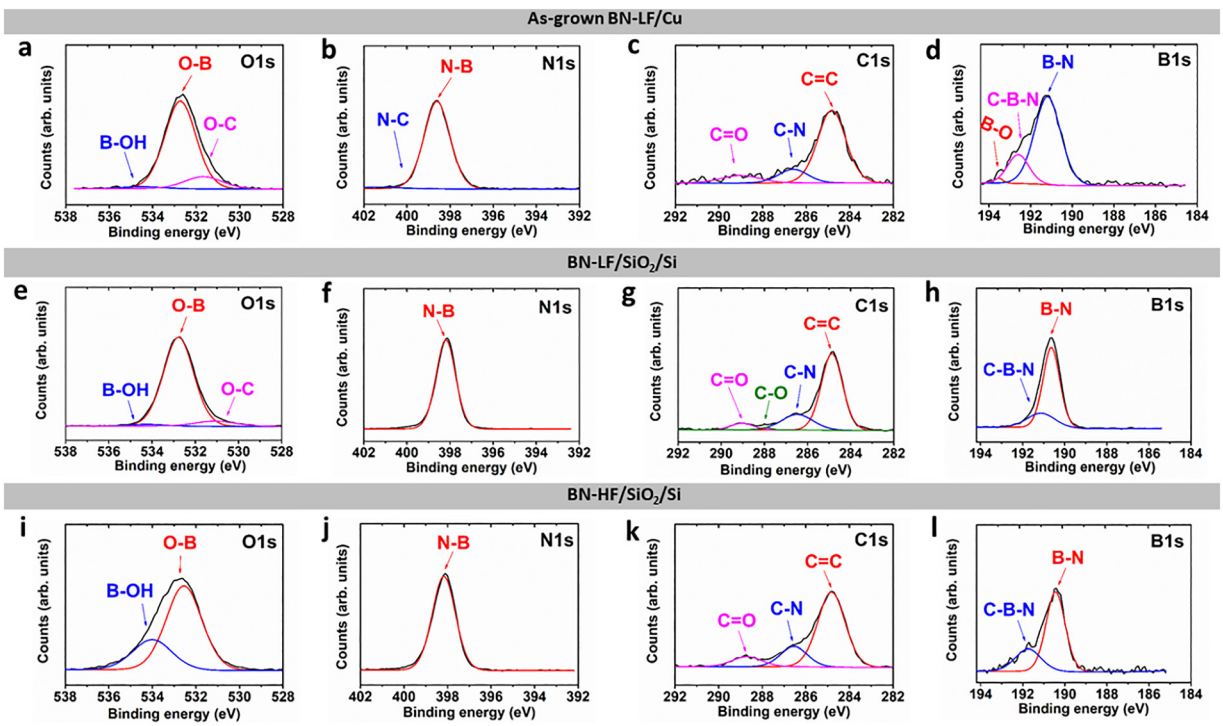

Fig. 5 (a)–(d) XPS spectra of as-grown BN-LF on Cu foil. (e)–(h) XPS scans of BN films transferred onto SiO_2/Si substrates for BN-LF/SiO_2/Si, and (i)–(l) for BN-HF/SiO_2/Si, together with peak fits for the various contributions (represented with red, blue, green, and magenta colors).

(Fig. 5h and l).[59,61] It is clear that the B–O bonds indicated in BN-LF/Cu (Fig. 5d) are not seen in BN LF(HF)/SiO_2/Si samples (Fig. 5h and l), signifying that boron–oxygen bonding (corresponding to B_2O_3 atomic defects) are gradually removed during the Cu etching in $FeCl_3$ solution and final cleaning process (acetone, IPA, and ultrasonication in DI water). Moreover, it is evident from the B 1s and N 1s spectra that the primary configuration of the B and N atoms in the samples BN-LF(HF)/SiO_2/Si is sp^2 B–N bonding.[54,58] Considering these variations in all samples, it is therefore highly possible that Cu etching in $FeCl_3$ solution, PMMA-based transfer process, and final cleaning steps at different solutions play a key role in fabricating high-quality and homogeneous thin BN films.

To better understand the heteroatom insertion in the BN lattice, XPS analysis is used to extract the atomic concentration of the different elements constituting the films (Table 2). Interestingly, the concentration of boron and nitrogen remain stable in the as grown BN-LF/Cu and BN-LF/SiO_2/Si samples. Contrariwise, the amount of nitrogen in BN-HF/SiO_2/Si is slightly increased compared to BN-LF/SiO_2/Si. Additionally, the boron concentration in this sample (BN-HF/SiO_2/Si) is strongly decreased, which may be expected during the main steps involved in the transfer of BN films onto a SiO_2/Si substrate by the wet chemical method indicated previously.

Table 2 displays the B/N ratio of BN-LF films calculated from the XPS analysis ($\sim$1.6 and 1.3), which are slightly higher than the stoichiometric ratio of h-BN in the literature.[62,63] In fact, these results attest that BN films are successfully developed, and the produced BN is mostly B-rich. However, this is not the case for BN-HF films transferred onto SiO_2/Si (B/N $\sim$ 0.4, *i.e.*, B-poor). This is a surprising observation, especially since the transfer process was conducted with the same conditions for both samples (BN-LF/SiO_2/Si and BN-HF/SiO_2/Si). In this context, the high flow rate of Ar (95 sccm) during the AB pre-treatment conducted for the BN-HF sample might explain this paradox; meaning that the feeding of B and N atoms at the end of the AP-CVD growth of the BN-HF films is not balanced.

3.5 Optical and structural analysis of BN films

To investigate the optical properties of the BN films, large-area ($\sim$1 cm^2) BN films are transferred to sapphire (Al_2O_3) substrates. It was difficult to control the transfer of these BN films because their transparency hinders its observation on the solutions and particularly in DI water (Fig. 6a). In fact, the transfer onto 1 cm^2 thin glass coverslips or sapphire is still challenging due to the small dimensions of the BN thin films and due to the transparency of these substrates (Fig. 6b). The uniformity and quality of BN on sapphire are studied by Raman spectroscopy. The BN-LF/sapphire thin films show an E_{2g} peak with homogeneous intensity over the surface, indicating thickness uniformity. The average position of the E_{2g} mode for BN-LF is 1370 cm^{-1} (FWHM $\sim$ 14 cm^{-1}),[64] indicating high uniformity of the BN films. Similarly, the Raman spectrum also shows a peak at 1376 cm^{-1} (FWHM $\sim$ 17 cm^{-1}), corresponding to sample BN-HF, as clearly depicted in Fig. 6c.

However, this Raman peak is less intense in BN-HF/sapphire films, indicating a possible slight decrease in number of BN layers in this sample. Here, it is important to emphasize that the Raman intensity corresponding to the E_{2g} peak characteristic of h-BN is proportional to the number of layers of boron nitride.[65,66] Additionally, the D and G peaks are registered at 1345 cm^{-1} and 1586 cm^{-1}, suggesting the presence of carbon contaminations. This is in agreement with the XPS results as seen in the previous section (carbon-containing impurities are indeed present in the studied BN films). XRR experiments are carried out to investigate the roughness and thickness of BN thin films. Following the fitting of the experimental XRR profiles (green and red curves), the dashed curves in Fig. 6d are generated. For BN-LF/sapphire and BN-HF/sapphire, thicknesses of (7.3 $\pm$ 0.1) nm and (6.3 $\pm$ 0.1) nm are measured, with a RMS surface roughness of 1.6 nm and 1.4 nm, respectively. The values are consistent with those from the AFM analysis (Fig. 4b and c). It is important to discern that there is a broad reflection near the $2\theta = 3^\circ$ grazing angle, which can be due to PMMA residues or unwanted impurities (see Fig. 6d, peak highlighted by an arrow). Furthermore, UV-vis spectroscopy is used to determine the transmittance and reflectance properties, aiming at determining the band gap energies of BN-LF and BN-HF on sapphire substrates, based on their optically induced direct-band transition. Fig. 6e displays a drop in transmittance between 190 and 240 nm. The band gap energy E_g is determined from transmittance data using the Tauc plot method, which can be expressed by the following eqn (1):[67,68]

$$(\alpha h\nu)^2 = A(h\nu - E_g) \quad (1)$$

where h is the Planck constant, α is the optical absorption coefficient, ν is the photon frequency, and A is the proportionality constant. Fig. 6f shows the $(\alpha h\nu)^2$ *versus* $h\nu$ curve acquired from the thin BN films on Al_2O_3. Even though their thicknesses are relatively similar, there is a significant change in the band gap. The measured optical energy gaps of BN films are significantly smaller than that of pristine hexagonal boron nitride ($\sim$6.0 eV), which indicates the presence of defect-mediated electronic states that introduce localized in-gap states and narrow the optical band gap. BN-LF exhibits a larger optical energy gap (5.02 $\pm$ 0.01 eV) compared to BN-HF (3.73 $\pm$ 0.02 eV and 4.64 $\pm$ 0.01 eV), suggesting a lower defect density in BN-LF films. Furthermore, BN-HF films display intermediate sub-band gap states, likely originating from various defects, strain, structural disorder in the material or impurity carriers located between the conduction and valence bands.[54,69]

Table 2 Atomic concentration of boron, nitrogen, and oxygen, as well as B/N ratios measured with XPS for as-grown BN-LF films on Cu foil and BN-LF (HF) on a SiO_2/Si substrates

Sample	O (%)	N (%)	B (%)	B/N
As-grown BN-LF/Cu	20.7	30.6	48.0	1.6
BN-LF/SiO_2/Si	23.7	33.8	42.4	1.3
BN-HF/SiO_2/Si	40.4	41.2	18.4	0.4

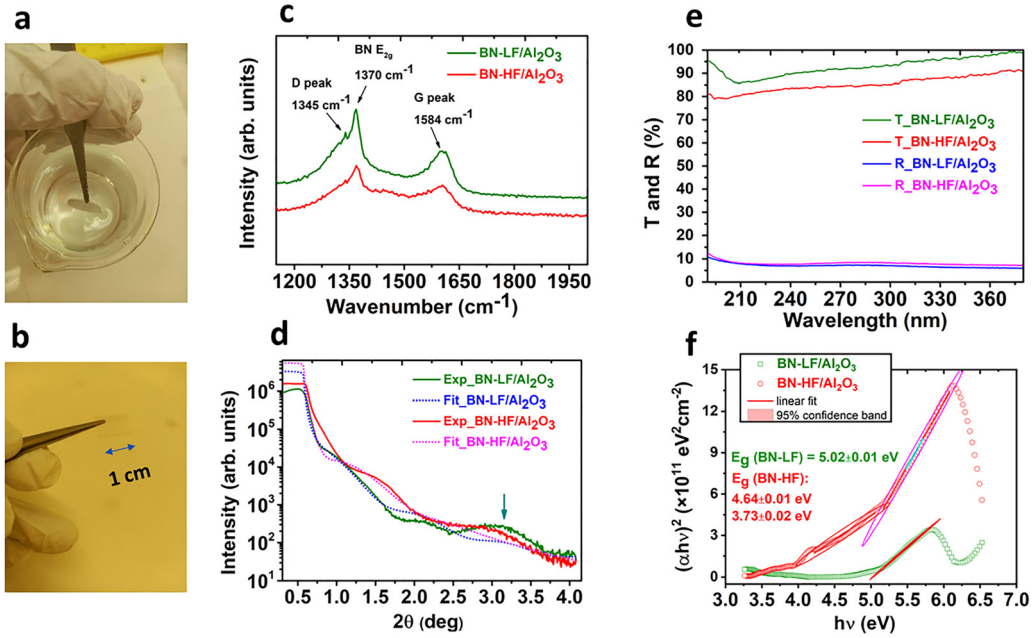

Fig. 6 (a) Photograph of the fishing step of BN films using a sapphire substrate. (b) Photograph of a large-area BN film (1 cm^2) on sapphire substrate after it is well-dried with nitrogen. (c) Raman spectra of BN films on sapphire substrates: BN-LF (green) and BN-HF (red), (d) XRR patterns of BN-LF and BN-HF films deposited on sapphire substrates (green and red lines, respectively) with corresponding fitted curves (blue and magenta). (e) Optical transmittance (green and red curves) and reflectance (blue and magenta curves) spectra of BN-LF and BN-HF on sapphire substrates, respectively. (f) Tauc plots for estimating optical band gap energies: BN-LF (5.02 ± 0.01 eV) and BN-HF (3.73–4.64 ± 0.01 eV).

3.6 Fluorescence intermittency study for BN films

Wide-field super-resolution microscopy (total internal reflection fluorescence: TIRF) is employed to illuminate the BN thin films. An evanescent wave is created by total internal reflection at the glass/film interface (Fig. 7a).

The emitted light from the sample is collected *via* the same objective and imaged onto an EMCCD camera. To analyze photon emission properties of the BN films, large-area BN films were transferred onto thin glass coverslips (0.13–0.16 mm thick). TIRF microscopy images are obtained by focusing a laser off-axis at the back focal plane of the objective, such that the emergent beam at the sample interface is near-collimated and incident at a greater angle than the critical angle for the glass/film interface. Fig. 7b shows a TIRF image example taken from a TIRF image sequence taken with an exposure time of 50 ms per frame for BN-LF film on glass coverslip when excited with a continuous-wave (CW) 488 nm laser at room temperature in air. This excitation of 488 nm (2.54 eV) is well below the band gap of h-BN (~6.0 eV) and does not excite the bulk h-BN material. However, it does interact with defect states in the band gap.[30,70] Fig. 7b shows highly magnified images for two different emitters with snapshots taken over an observation period of 90 s, revealing temporal variations in their emission brightness. The first emitter (E1) shows a high brightness with minor variations with 90 seconds recording of the emission intensity. In contrast, the second emitter (E2) exhibits less brightness with a large variation in emission intensity, as observed after the first 30 s (5 s increment). In addition, Fig. S6 presents a TIRF optical image with the identified spatial distribution of photon emitters in a region of interest from the BN-LF film; this super-resolved 8 μm^2 image presents the localization of optically active photon emitters (SI). Fig. 7d and e present photon emission fluctuations from selected emitters in the BN-LF thin films during an observation period of 120 s.

By using the ThunderSTORM plugin in ImageJ software followed by a threshold analysis, the fluorescence intensity trajectory for emitters in Fig. 7e shows well-defined "ON" and "OFF" levels.[71] Interestingly, the emitters in BN-HF films display stronger fluorescence intermittency (blinking) compared with those in BN-LF (Fig. 7d). This is probably consistent with having distinct energy gaps in the sample BN-HF, as derived from the optical spectrophotometry measurements (Fig. 6f). The histograms in Fig. 7f and g resulting from the photon counts show the distribution of intensity values across the whole time trace, revealing an evident distinction between bright and dark states in both samples. Hence, the photon emitters described with "ON" and "OFF" blinking from the BN films are likely to derive from various atomic-scale defects such as strain, adatoms, cracks, grain boundaries or vacancies.

The TIRF study shows that the BN-LF and BN-HF thin films exhibit fluorescent emitters at room temperature. In this regard, hyperspectral confocal fluorescence microscopy (HCFM) data can provide a quantitative analysis of fluorescence emission at specific excitation. It can also measure the distribution of different spectral features associated with the pixel color in the recorded hyperspectral images. However, this method has limitations for large-area characterization due to the time required for scanning. The spatial distribution of the

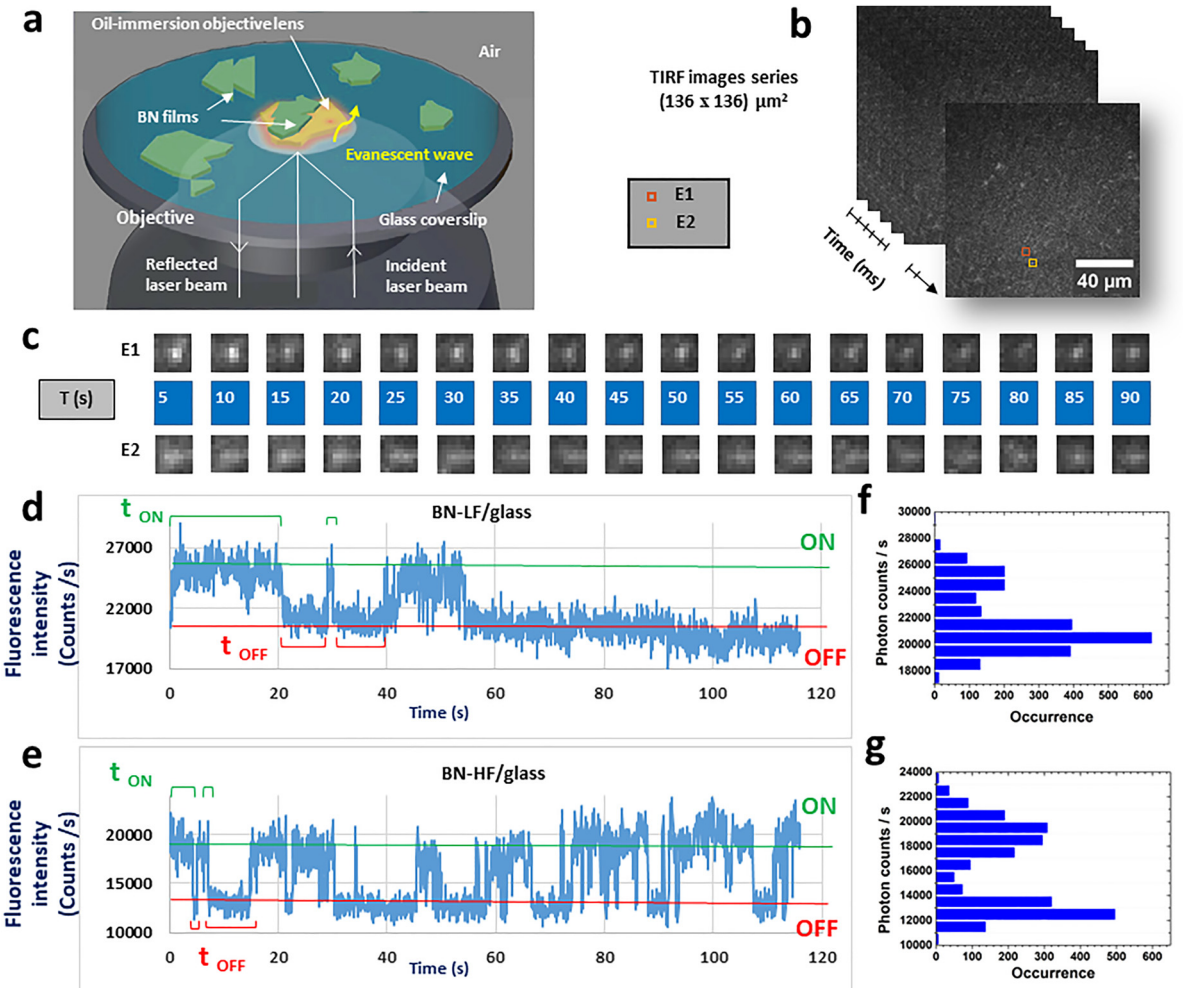

Fig. 7 (a) Total internal reflection fluorescence setup used for BN thin films on glass coverslips, excited with CW laser light of 488 nm. (b) TIRF microscopy image of a few multilayers of BN-LF taken from a TIRF image series; (c) zoomed-in images of two different photon emitters (E1: highly bright emitter; E2: less bright emitter) showing temporal variations in emission brightness during 90 s (5 s increments). The square size is 2.14 μm^2. Fluorescence intensities are plotted as photon counts over time: fluorescence trajectories of a photon emitter in (d) BN-LF thin films and (e) BN-HF thin films, showing fluctuations between "ON" and "OFF" states (green and red lines are guides to the eye) representing the photon counts for the emissive and non-emissive thresholds. (f) and (g) Are the corresponding count rate occurrence histograms of the two distinct states ("ON" and "OFF") for the two BN thin films.

transferred BN films on glass coverslip is not necessarily fully uniform, which makes the analysis more complex while scanning various areas. To evaluate the utility of this imaging technique, the system is employed to scan an area of 45 μm × 12 μm of the BN thin films on glass coverslips. Fig. 8a and b present the hyperspectral confocal fluorescence images using an electron multiplied charge coupled device camera (EMCCD), showing the distribution of fluorescent spots of the BN-LF and BN-HF films, respectively. The observed fluorescent spots appear as multiple circles or half-circles matching approximately the size of a single PSF. Significant fluorescence emissions ascribed to defects with zero phonon lines (ZPL) are observed more in the BN-HF film compared to those identified for the BN-LF film. Fig. 8c shows three emission peaks from the BN-LF film yielding ZPL positions at 555, 590, and 608 nm, respectively. In contrast, the BN-HF film displays six emission peaks with the corresponding ZPL with positions centered at 555, 564, 582, 600, 608, and 617 nm (Fig. 8d). The different emission wavelengths can be attributed to strain defects, presence of diverse substitutions of (O, H, and C atoms),[12,72] or due to N or B vacancies[60,73] and N_BV_N anti-site defects in the h-BN lattice.[30,74] In addition to the normalized spectra from various bright fluorescence spots in both samples presented in Fig. 8a and b, there are two emission peaks (red for BN-LF; violet for BN-HF), yielding a ZPL position at ~608 nm and a phonon sideband (PSB) centered at ~661 nm (see Fig. 8c and d). This corresponds to an energy detuning of ~170 meV between the ZPL and PSB, consistent with prior literature on h-BN defects which might be a possible origin of point defect-based SPEs at room temperature.[75,76] Interestingly, the BN-HF film exhibits photon emitters (color centers) with reproducible emissions under the same excitation wavelength (488 nm). As shown in Fig. S7, the zoomed-in hyperspectral confocal fluorescence image (BN-HF/glass) reveals several

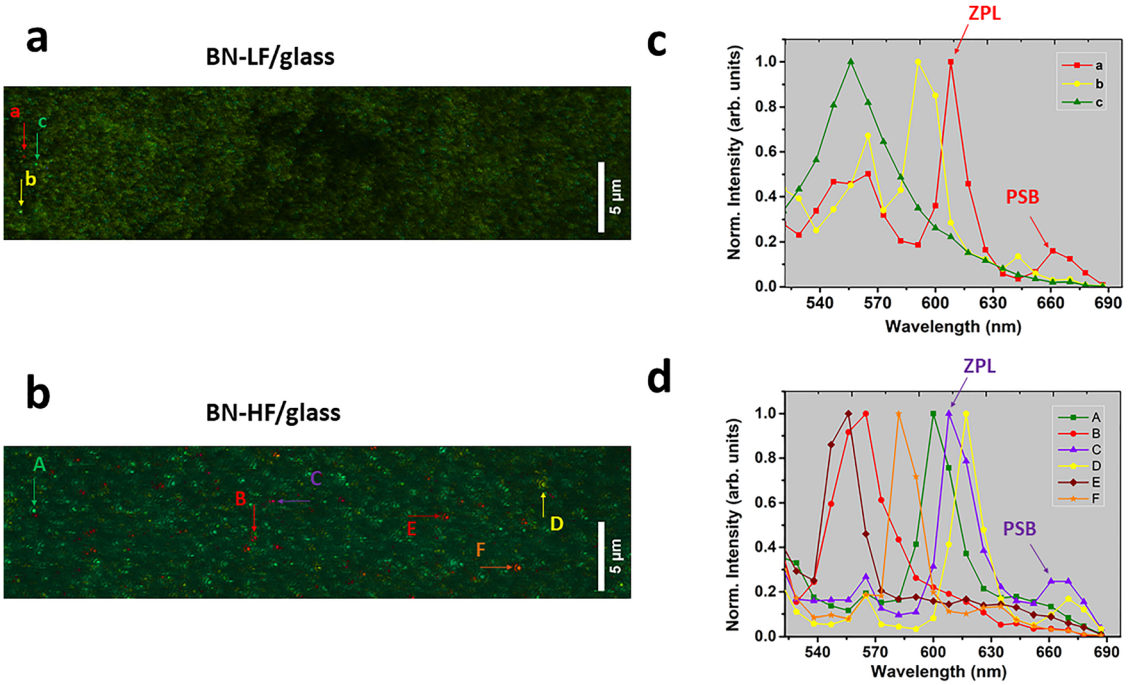

Fig. 8 (a) Zoomed-in hyperspectral confocal fluorescent images with bright spots labelled as: a, b, and c seen in the BN-LF films and with (b) A, B, C, D, E, and F seen in the BN-HF films. Normalized fluorescence spectra *versus* wavelength for (c) three examples of fluorescent spots in the BN-LF films with ZPLs at: 555 nm (2.23 eV), 590 nm (2.10 eV), and 608 nm (2.03 eV). For spectra illustrated in (d), six examples of bright spots (color centers) in the BN-HF films with ZPLs are observed at: 555 nm (2.23 eV), 564 nm (2.19 eV), 582 nm (2.13 eV), 600 nm (2.06 eV), 608 nm (2.03 eV), and 617 nm (2.00 eV). ZPL and PSB refer to zero-phonon line and phonon side band, respectively.

emitters displaying similar colors (see SI for details). Additionally, multiple emission peaks show identical narrow zero-phonon lines (ZPLs), accompanied by various broader phonon side bands (PSBs) at larger wavelengths. We predict that the slight differences in emissions arise from variations in the degree of strain induced in the BN films during the growth and/or transfer process. The SPE density in CVD h-BN varies widely in the literature, with reports ranging from 0.009 emitters per μm^2 (ref. 77) to 2.2 emitters per μm^2.[78] The emitter density in our BN thin films are quantified from hyperspectral confocal fluorescent images (Fig. 8a and b). Photon emitters in BN-LF are distributed at a low density of (0.06 ± 0.01) emitters per μm^2, while the BN-HF film exhibit a slightly larger density of (0.09 ± 0.01) emitters per μm^2 (Fig. S8 in SI). These findings highlight the strong SPE signature of BN-HF thin film and its potential for quantum photonic applications.

4. Conclusions

The synthesis of 2D BN grown by AP-CVD under two different Ar flow conditions during the AB pre-treatment process (low and high flow rates) results in continuous and large-area islands. The thickness of BN-LF and BN-HF films is approximately 7 nm, as determined by AFM and XRR studies. XPS results provide chemical bonding information and confirm that both BN-LF and BN-HF films display similar chemical contributions, with B/N ratios between 1.3 and 1.6, particularly in BN-LF. The BN thin films produced in this work exhibit band gap energies between 3.73 and 5.02 eV, which vary due to various possible defect states. Moreover, the fluorescence intensity trajectories of emitters in BN films show well-defined "ON" and "OFF" levels in spectrally-resolved fluorescence imaging, attributed to the blinking effect of room temperature photon emitters. Future second-order auto-correlation of photon distribution measurements could be a promising approach to achieve spatial control of SPEs and confirm their purity. Finally, AB thermal decomposition under Ar flow is shown to be a crucial step for the large-scale synthesis of BN thin films. Its behavior needs to be well understood for the optimization of AP-CVD h-BN growth. The findings of this study can promote the development of 2D materials for electronics and future optical quantum applications.

Author contributions

EA, SS, and CJT: conceptualization; EA, TQ, JCP, CJT, and DAG: investigation and methodology; EA, NN, JBN, and SSN: formal analysis; CJT and SS: supervision and validation; CJT, PA, and SS: funding acquisition; EA, TQ, and CJT: writing – original draft; EA, TQ, PA, CJT, and SS: writing – review & editing.

Conflicts of interest

There are no conflicts to declare.

Data availability

The data and figures generated and/or analysed during this study are available from the corresponding author upon request.

Supplementary information (SI) is available. See DOI: https://doi.org/10.1039/d5ma00584a.

Acknowledgements

This research was supported by Fundação para a Ciência e Tecnologia (FCT, Portugal) for the PhD grant (PRT/BD/151555/2021) under the ''Quantum Portugal Initiative'' Program. We acknowledge the access and support from the Materials Characterization Services Laboratory of the University of Minho (SEMAT/UM), 2D materials and the Nanophotonics and Bioimaging (NBI) and Micro and Nano Fabrication (MNF) core facilities of INL. We also acknowledge Prof. Katharina Lorenz (IPFN, Instituto Superior Técnico, University of Lisbon) for the fruitful discussion. This work was supported by the Portuguese Foundation for Science and Technology (FCT) in the framework of the Strategic Funding UID/04650/2025, https://doi.org/10.54499/UID/04650/2025.

References

1 W. Olovsson and M. Magnuson, *J. Phys. Chem. C*, 2022, **126**, 21101–21108.
2 J. Iwański, K. P. Korona, M. Tokarczyk, G. Kowalski, A. K. Dąbrowska, P. Tatarczak, I. Rogala, M. Bilska, M. Wójcik, S. Kret, A. Reszka, B. J. Kowalski, S. Li, A. Pershin, A. Gali, J. Binder and A. Wysmołek, *npj 2D Mater. Appl.*, 2024, **8**, 72.
3 C. R. Dean, A. F. Young, I. Meric, C. Lee, L. Wang, S. Sorgenfrei, K. Watanabe, T. Taniguchi, P. Kim, K. L. Shepard and J. Hone, *Nat. Nanotechnol.*, 2010, **5**, 722–726.
4 Z. Xu, H. Tian, A. Khanaki, R. Zheng, M. Suja and J. Liu, *Sci. Rep.*, 2017, **7**, 43100.
5 Z. Zhu, Z. Zhang, S. Wang, J. Zou, Y. Gan, R. Yang, Y. Zhang and B. Long, *Cryst. Growth Des.*, 2023, **23**, 7662–7668.
6 L. Song, L. Ci, H. Lu, P. B. Sorokin, C. Jin, J. Ni, A. G. Kvashnin, D. G. Kvashnin, J. Lou, B. I. Yakobson and P. M. Ajayan, *Nano Lett.*, 2010, **10**, 3209–3215.
7 W. Yang, G. Chen, Z. Shi, C. C. Liu, L. Zhang, G. Xie, M. Cheng, D. Wang, R. Yang, D. Shi, K. Watanabe, T. Taniguchi, Y. Yao, Y. Zhang and G. Zhang, *Nat. Mater.*, 2013, **12**, 792–797.
8 S. K. Jang, J. Youn, Y. J. Song and S. Lee, *Sci. Rep.*, 2016, **6**, 1–9.
9 H. Agarwal, B. Terrés, L. Orsini, A. Montanaro, V. Sorianello, M. Pantouvaki, K. Watanabe, T. Taniguchi, D. Van Thourhout, M. Romagnoli and F. H. L. Koppens, *Nat. Commun.*, 2021, **12**, 8–13.
10 Z. Ma, C. Prawoto, Z. Ahmed, Y. Xiao, L. Zhang, C. Zhou and M. Chan, *J. Mater. Chem. C*, 2019, **7**, 6273–6278.
11 S. S. Chng, M. Zhu, J. Wu, X. Wang, Z. K. Ng, K. Zhang, C. Liu, M. Shakerzadeh, S. Tsang and E. H. T. Teo, *J. Mater. Chem. C*, 2020, **8**, 4421–4431.
12 D. Zhong, S. Gao, M. Saccone, J. R. Greer, M. Bernardi, S. Nadj-Perge and A. Faraon, *Nano Lett.*, 2024, **24**, 1106–1113.
13 D. Lee and S. H. Song, *RSC Adv.*, 2017, **7**, 7831–7835.
14 X. Song, Q. Li, J. Ji, Z. Yan, Y. Gu, C. Huo, Y. Zou, C. Zhi and H. Zeng, *2D Mater.*, 2016, **3**, 035007.
15 G. A. Alvarez, J. Christiansen-Salameh, A. Biswas, A. B. Puthirath, E. Jeong, J. Kwon, J. Lee, T. Gray, R. Vajtai, P. M. Ajayan and Z. Tian, *Appl. Phys. Lett.*, 2023, **122**, 232101.
16 H. Yin, X. Zhang, J. Lu, X. Geng, Y. Wan, M. Wu and P. Yang, *J. Mater. Sci.*, 2020, **55**, 7701.
17 B. Liu, M. Fathi, L. Chen, A. Abbas, Y. Ma and C. Zhou, *ACS Nano*, 2015, **9**, 6119–6127.
18 H. Bergeron, V. K. Sangwan, J. J. McMorrow, G. P. Campbell, I. Balla, X. Liu, M. J. Bedzyk, T. J. Marks and M. C. Hersam, *Appl. Phys. Lett.*, 2017, **110**, 053101.
19 R. Guan, J. Duan, A. Yuan, Z. Wang, S. Yang, L. Han, B. Zhang, D. Li and B. Luo, *CrystEngComm*, 2021, **23**, 146–152.
20 X. Wang, X. Shi, C. Gu, Q. Guo, H. Liu, X. Li and Y. Wu, *APL Mater.*, 2021, **9**, 1–7.
21 Z. Liu, Y. Gong, W. Zhou, L. Ma, J. Yu, J. C. Idrobo, J. Jung, A. H. MacDonald, R. Vajtai, J. Lou and P. M. Ajayan, *Nat. Commun.*, 2013, **4**, 2541.
22 X. Yang, M. Pristovsek, S. Nitta, Y. Honda, A. Ohtake, Y. Sakuma, T. Hiroto, T. Ishida, M. Ikezawa, Q. Guo and H. Amano, *Adv. Sci.*, 2025, **12**, e09354.
23 M. Shanmugam, R. Jacobs-Gedrim, C. Durcan and B. Yu, *Nanoscale*, 2013, **5**, 11275–11282.
24 H. Liu, J. Meng, X. Zhang, Y. Chen, Z. Yin, D. Wang, Y. Wang, J. You, M. Gao and P. Jin, *Nanoscale*, 2018, **10**, 5559–5565.
25 S. B. Song, S. Yoon, S. Y. Kim, S. Yang, S. Y. Seo, S. Cha, H. W. Jeong, K. Watanabe, T. Taniguchi, G. H. Lee, J. S. Kim, M. H. Jo and J. Kim, *Nat. Commun.*, 2021, **12**, 4–12.
26 N. Mendelson, M. Doherty, M. Toth, I. Aharonovich and T. T. Tran, *Adv. Mater.*, 2020, **32**, 1–9.
27 X. Chen, X. Yue, L. Zhang, X. Xu, F. Liu, M. Feng, Z. Hu, Y. Yan, J. Scheuer and X. Fu, *Adv. Funct. Mater.*, 2024, **34**, 1–10.
28 Z.-Q. Xu, C. Elbadawi, T. T. Tran, M. Kianinia, X. Li, D. Liu, T. B. Hoffman, M. Nguyen, S. Kim, J. H. Edgar, X. Wu, L. Song, S. Ali, M. Ford, M. Toth and I. Aharonovich, *Nanoscale*, 2018, **10**, 7957–7965.
29 A. Carbone, I. D. Breev, J. Figueiredo, S. Kretschmer, L. Geilen, A. Ben Mhenni, J. Arceri, A. V. Krasheninnikov, M. Wubs, A. W. Holleitner, A. Huck, C. Kastl and N. Stenger, *Phys. Rev. Mater.*, 2025, **9**, 056203.
30 T. T. Tran, K. Bray, M. J. Ford, M. Toth and I. Aharonovich, *Nat. Nanotechnol.*, 2016, **11**, 37–41.
31 H. Liu, N. Mendelson, I. H. Abidi, S. Li, Z. Liu, Y. Cai, K. Zhang, J. You, M. Tamtaji, H. Wong, Y. Ding, G. Chen, I. Aharonovich and Z. Luo, *ACS Appl. Mater. Interfaces*, 2022, **14**, 3189–3198.
32 M. Fischer, J. M. Caridad, A. Sajid, S. Ghaderzadeh, M. Ghorbani-Asl, L. Gammelgaard, P. Bøggild, K. S. Thygesen, A. V. Krasheninnikov, S. Xiao, M. Wubs and N. Stenger, *Sci. Adv.*, 2021, **7**, 1–8.

33 R. Y. Tay, X. Wang, S. H. Tsang, G. C. Loh, R. S. Singh, H. Li, G. Mallick and E. H. Tong Teo, *J. Mater. Chem. C*, 2014, **2**, 1650.
34 J. C. Koepke, J. D. Wood, Y. Chen, S. W. Schmucker, X. Liu, N. N. Chang, L. Nienhaus, J. W. Do, E. A. Carrion, J. Hewaparakrama, A. Rangarajan, I. Datye, R. Mehta, R. T. Haasch, M. Gruebele, G. S. Girolami, E. Pop and J. W. Lyding, *Chem. Mater.*, 2016, **28**, 4169–4179.
35 V. Babenko, G. Lane, A. A. Koos, A. T. Murdock, K. So, J. Britton, S. S. Meysami, J. Moffat and N. Grobert, *Sci. Rep.*, 2017, **7**, 14297.
36 S. Behura, P. Nguyen, S. Che, R. Debbarma and V. Berry, *J. Am. Chem. Soc.*, 2015, **137**, 13060–13065.
37 K. Ba, W. Jiang, J. Cheng, J. Bao, N. Xuan, Y. Sun, B. Liu, A. Xie, S. Wu and Z. Sun, *Sci. Rep.*, 2017, **7**, 45584.
38 Y. Gao, W. Ren, T. Ma, Z. Liu, Y. Zhang, W.-B. Liu, L.-P. Ma, X. Ma and H.-M. Cheng, *ACS Nano*, 2013, **7**, 5199–5206.
39 S. Sharma, G. Kalita, R. Vishwakarma, Z. Zulkifli and M. Tanemura, *Sci. Rep.*, 2015, **5**, 10426.
40 J. Fernandes, T. Queirós, J. Rodrigues, S. S. Nemala, A. P. LaGrow, E. Placidi, P. Alpuim, J. B. Nieder and A. Capasso, *FlatChem*, 2022, **33**, 1–12.
41 I. Vlassiouk, M. Regmi, P. Fulvio, S. Dai, P. Datskos, G. Eres and S. Smirnov, *ACS Nano*, 2011, **5**, 6069–6076.
42 Q. Wu, J.-H. Park, S. Park, S. J. Jung, H. Suh, N. Park, W. Wongwiriyapan, S. Lee, Y. H. Lee and Y. J. Song, *Sci. Rep.*, 2015, **5**, 16159.
43 S. Frueh, R. Kellett, C. Mallery, T. Molter, W. S. Willis, C. King'ondu and S. L. Suib, *Inorg. Chem.*, 2011, **50**, 783–792.
44 B. Roy, J. Manna and P. Sharma, *J. Alloys Compd.*, 2015, **645**, 234–238.
45 Q. Lai, A. Rawal, Z. Quadir, C. Cazorla and U. B. Demirci, *Adv. Sustainable Syst.*, 2018, **2**, 1–14.
46 Y. Lin, W. L. Mao, V. Drozd, J. Chen and L. L. Daemen, *J. Chem. Phys.*, 2008, **129**, 234509.
47 U. B. Demirci, *Int. J. Hydrogen Energy*, 2017, **42**, 9978–10013.
48 M. H. Khan, Z. Huang, F. Xiao, G. Casillas, Z. Chen, P. J. Molino and H. K. Liu, *Sci. Rep.*, 2015, **5**, 21–24.
49 M. A. Kriegel, K. M. Omambac, S. Franzka, F. J. Meyer zu Heringdorf and M. Horn-von Hoegen, *Appl. Surf. Sci.*, 2023, **624**, 1–5.
50 K. K. Kim, A. Hsu, X. Jia, S. M. Kim, Y. Shi, M. Hofmann, D. Nezich, J. F. Rodriguez-Nieva, M. Dresselhaus, T. Palacios and J. Kong, *Nano Lett.*, 2012, **12**, 161–166.
51 H. Li, S. Zhu, M. Zhang, P. Wu, J. Pang, W. Zhu, W. Jiang and H. Li, *ACS Omega*, 2017, **2**, 5385–5394.
52 C. Zhang, S. Zhao, C. Jin, A. L. Koh, Y. Zhou, W. Xu, Q. Li, Q. Xiong, H. Peng and Z. Liu, *Nat. Commun.*, 2015, **6**, 1–8.
53 V. Jain, M. C. Biesinger and M. R. Linford, *Appl. Surf. Sci.*, 2018, **447**, 548–553.
54 A. Sunny, A. Balapure, R. Ganesan and R. Thamankar, *ACS Omega*, 2022, **7**, 33926–33933.
55 B. J. Matsoso, K. Ranganathan, B. K. Mutuma, T. Lerotholi, G. Jones and N. J. Coville, *New J. Chem.*, 2017, **41**, 9497–9504.
56 S. Wan, Y. Yu, J. Pu and Z. Lu, *RSC Adv.*, 2015, **5**, 19236–19240.
57 Q. Li, X. Qin, Q. Zhang, Y. Bai, H. Tang, C. Hu, S. Shen, Y. Li and F. Yun, *J. Mater. Res.*, 2020, **35**, 3247–3256.
58 A. C. Khot, T. D. Dongale, K. A. Nirmal, J. H. Sung, H. J. Lee, R. D. Nikam and T. G. Kim, *ACS Appl. Mater. Interfaces*, 2022, **14**, 10546–10557.
59 L. H. Li, T. Xing, Y. Chen and R. Jones, *Adv. Mater. Interfaces*, 2014, **1**, 1–6.
60 S. X. Li, T. Ichihara, H. Park, G. He, D. Kozawa, Y. Wen, V. B. Koman, Y. Zeng, M. Kuehne, Z. Yuan, S. Faucher, J. H. Warner and M. S. Strano, *Commun. Mater.*, 2023, **4**, 1–11.
61 Y. Chen, X. Xu, C. Li, A. Bendavid, M. T. Westerhausen, C. Bradac, M. Toth, I. Aharonovich and T. T. Tran, *Small*, 2021, **17**, 1–7.
62 Y. Chen, H. Liang, X. Xia, H. Zhang and J. Shi, *J. Mater. Sci.: Mater. Electron.*, 2017, **28**, 14341–14347.
63 M. Yamamoto, H. Murata, N. Miyata, H. Takashima, M. Nagao, H. Mimura, Y. Neo and K. Murakami, *ACS Omega*, 2023, **8**, 5497–5505.
64 Y. Yang and W. Sun, *Phys. Scr.*, 2023, **98**, 125989.
65 F. Schaumburg, S. Sleziona, M. Zöllner, V. Dergianlis, M. Schleberger, M. Geller, A. Lorke and G. Prinz, *Appl. Phys. Lett.*, 2023, **123**, 073101.
66 R. V. Gorbachev, I. Riaz, R. R. Nair, R. Jalil, L. Britnell, B. D. Belle, E. W. Hill, K. S. Novoselov, K. Watanabe, T. Taniguchi, A. K. Geim and P. Blake, *Small*, 2011, **7**, 465–468.
67 J. Tauc, R. Grigorovici and A. Vancu, *Phys. Status Solidi*, 1966, **15**, 627–637.
68 M. Toma, N. Ursulean, D. Marconi and A. Pop, *J. Electr. Eng.*, 2019, **70**, 127–131.
69 R. Sevak Singh, R. Yingjie Tay, W. Leong Chow, S. Hon Tsang, G. Mallick and E. H. Tong Teo, *Appl. Phys. Lett.*, 2014, **104**, 163101–163104.
70 C. Attaccalite, M. Bockstedte, A. Marini, A. Rubio and L. Wirtz, *Phys. Rev. B: Condens. Matter Mater. Phys.*, 2011, **83**, 1–8.
71 H. L. Stern, R. Wang, Y. Fan, R. Mizuta, J. C. Stewart, L. M. Needham, T. D. Roberts, R. Wai, N. S. Ginsberg, D. Klenerman, S. Hofmann and S. F. Lee, *ACS Nano*, 2019, **13**, 4538–4547.
72 S. Li and A. Gali, *J. Phys. Chem. Lett.*, 2022, **13**, 9544–9551.
73 A. Kumar, Ç. Samaner, C. Cholsuk, T. Matthes, S. Paçal, Y. Oyun, A. Zand, R. J. Chapman, G. Saerens, R. Grange, S. Suwanna, S. Ateş and T. Vogl, *ACS Nano*, 2023, **18**, 5270–5281.
74 G. Grosso, H. Moon, B. Lienhard, S. Ali, D. Efetov, M. M. Furchi, P. Jarillo-Herrero, M. J. Ford, I. Aharonovich and D. Englund, *Nat. Commun.*, 2017, **8**, 1–8.
75 C. Li, N. Mendelson, R. Ritika, Y. Chen, Z. Q. Xu, M. Toth and I. Aharonovich, *Nano Lett.*, 2021, **21**, 3626–3632.
76 T. T. Tran, C. Elbadawi, D. Totonjian, C. J. Lobo, G. Grosso, H. Moon, D. R. Englund, M. J. Ford, I. Aharonovich and M. Toth, *ACS Nano*, 2016, **10**, 7331–7338.
77 Y. Chen, C. Li, S. White, M. Nonahal, Z.-Q. Xu, K. Watanabe, T. Taniguchi, M. Toth, T. T. Tran and I. Aharonovich, *ACS Appl. Mater. Interfaces*, 2021, **13**, 47283–47292.
78 N. Mendelson, Z.-Q. Xu, T. T. Tran, M. Kianinia, J. Scott, C. Bradac, I. Aharonovich and M. Toth, *ACS Nano*, 2019, **13**, 3132–3140.